

Nanoscale

Accepted Manuscript



This is an *Accepted Manuscript*, which has been through the Royal Society of Chemistry peer review process and has been accepted for publication.

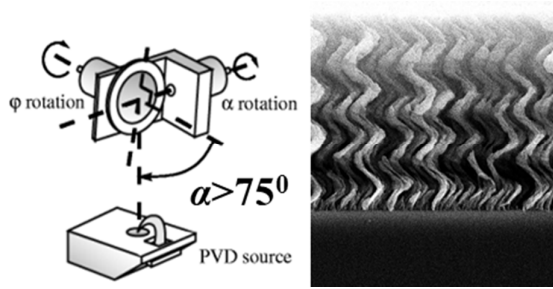
Accepted Manuscripts are published online shortly after acceptance, before technical editing, formatting and proof reading. Using this free service, authors can make their results available to the community, in citable form, before we publish the edited article. We will replace this *Accepted Manuscript* with the edited and formatted *Advance Article* as soon as it is available.

You can find more information about *Accepted Manuscripts* in the [Information for Authors](#).

Please note that technical editing may introduce minor changes to the text and/or graphics, which may alter content. The journal's standard [Terms & Conditions](#) and the [Ethical guidelines](#) still apply. In no event shall the Royal Society of Chemistry be held responsible for any errors or omissions in this *Accepted Manuscript* or any consequences arising from the use of any information it contains.

Table of contents:

Helical porous thin films obliquely deposited are reviewed in terms of fabrication, growth mechanism, physical properties and applications in green energy.



Wafer-scale, Three-Dimensional Helical Porous Thin Films Deposited at a Glancing Angle

Zhifeng Huang,^{*1,2,3} and Fan Bai¹

¹Department of Physics, ²Institute of Advanced Materials, Hong Kong Baptist University (HKBU), Kowloon Tong, Hong Kong SAR, P. R. China

³HKBU Institute of Research and Continuing Education, A211, Virtual University Park Building, South Area Hi-tech Industrial Park, Shenzhen, Guangdong Province, P. R. China

Abstract:

Minimization of helices opens a door to impose novel functions derived from the dimensional shrinkage onto optical, mechanical and electronic devices. Glancing angle deposition (GLAD) enables one to deposit three-dimensional helical porous thin films (HPTFs) composed of separated spiral micro/nano-columns. GLAD integrates a series of advantageous features, including one-step deposition, wafer-scale production with mono-handedness, flexible engineering of spiral materials and dimensions, and the adaptation to various kinds of substrates. Herein, we briefly review the fabrication of HPTFs by GLAD, specific growth mechanism, physical properties in structures, mechanics and chiral optics, and the emerging applications in green energy. A prospective outlook is presented to illuminate some promising developments in enantioselection, bio-dynamic analyses, wirelessly-controlled drug delivery and mass production.

1. Introduction

Spiral coils are of practical interest owing to an integration of coil handedness, elastic mechanical properties, optical functions and rotary propagation. Minimization of spirals has been being pursued in order to impose dimension-determined new properties onto small spirals for functioning electrical, optical and mechanical devices in the micro/nano scales.¹ Among various fabrication techniques developed to generate small springs, glancing angle deposition (GLAD) can create three-dimensional helical porous thin films (HPTFs) made of an array of separated spiral micro/nano-columns, and has a series of advantages over other methods. First, GLAD creates HPTFs via one-step deposition. Second, GLAD can deposit HPTFs on a 4- or 6-inch wafer in a fairly uniform way. Third, there is no mixture of left and right handedness in a HPTF, that is, HPTFs contain only one chirality. Fourth, GLAD can flexibly engineer the spiral dimensions from micro- to nano-scales by carefully controlling a set of experimental conditions. Fifth, GLAD is adapted to a wide variety of materials, including low- T_m (T_m : melting point) materials (e.g. Ag,² Au,³ Cu,⁴ Al,⁵ Ge,⁶ Tris(8-hydroxyquinolino)aluminium,⁷ C60,⁸ zinc phthalocyanine⁹) and high- T_m species (e.g. Si,¹⁰ SiO₂,¹¹ TiO₂,¹² Al₂O₃,¹³ ZrO₂,¹⁴ HfO₂,¹⁵ MgF₂,¹⁶ indium tin oxide,¹⁷ InN,¹⁸ WO₃,¹⁹ Ta,²⁰ W,²¹ Fe,²² Cr,²³ Co²⁴). Sixth, HPTFs can be deposited onto various substrates, such as opaque Si wafers, visible-transparent substrates (glasses and ITO-coated glasses), UV-visible-transparent substrates (sapphires and quartz) and flexible adhesives, leading to wide adaption to diverse applications.

GLAD can sculpture porous thin films in various shapes, such as vertical posts, oblique posts, zigzags and (square) spirals.⁴ Compared to the others, spiral structures tend to have some merits. First, HPTFs have left- and right-handed chirality, which can be used for optical rotation, circular polarization and bio-enantioselection. Second,

since HPTFs have special mechanical properties of harmonic springs, the electric-mechanic-optic coupling can be operated to develop the applications in actuators and interferometers. Third, spirals are resistant to mechanical compression so that HPTFs can be transferred by an adhesive and attached to a wide range of substrates, which makes it widely adapted to diverse optical and mechanical applications. Herein we will briefly review the growth mechanism of HPTFs via GLAD, HPTFs' physical properties, and applications in green energy, and have an outlook of prospects. The applications of GLAD-generated HPTFs have been previously reviewed in terms of chromatography,²⁵ cholesteric liquid crystals,²⁶ chemical and biological sensors,²⁷ and diverse optical applications.²⁸⁻³⁰ Global environmental problems give rise to increasing concern about the employment of green energy, and this mini review will mainly focus on the emerging development of HPTFs in this field.

2. Fabrication

2.1 GLAD of HPTFs

GLAD is a physical vapor deposition at a highly oblique deposition angle ($\alpha > 75^\circ$) with respect to the substrate normal (Scheme 1a).³¹ The shape of PTFs is sculptured by controlling substrate movement during deposition, i.e. engineering the time dependence of azimuth angle φ (Scheme 1a). The clockwise spin generates right-handed helices, and the anticlockwise creates left handedness.³² GLAD can produce polygonal spirals, which have a projection of a pitch on the plane perpendicular to the longitudinal axis in a polygonal shape. The sculpture of polygonal helices is controlled by³³

$$\Delta\varphi = \frac{360^\circ}{m} \quad (1)$$

where $\Delta\varphi$ is the azimuth angle at which a deposited substrate is abruptly rotated each time in a circle of 360° , and m is the number of arms contained in a pitch of polygonal helices. Within the interval between two abrupt rotations, HPTFs grow in a thickness of P/m where P is the thickness of a pitch (Scheme 2c). For instance, a triangle helix is created when $m=3$ (Scheme 2), and a square spring is deposited while $m=4$ (Fig. 1). When m is increased to be infinite, $\Delta\varphi$ approaches to zero, leading to the deposition of a circular helix by rotating the substrate smoothly and unidirectionally (Fig. 2). Among a series of spiral dimensions of circular helices (Fig. 2a), P and n are in ease of experimental engineering. The deposition can be precisely controlled by³⁴

$$P = 120\pi \frac{r_d}{r_r} \quad (2)$$

where P is the spiral pitch in unit of $\text{nm}/(2\pi \text{ revolution})$, r_d is the deposition rate in unit of nm/s , and r_r is the rate of substrate rotation in unit of revolution per minute (rpm). Given by r_d that is suitable for deposited materials and targeted P , the substrate will be spun in a rate of r_r evaluated by eq. 2, which is typically far slower than 1 rpm. During GLAD r_d tends to have instant, unexpected fluctuation, especially for some oxides with high melting point, such as SiO_2 , ITO (indium tin oxide) and Al_2O_3 . In order to obtain a homogenous distribution of P along the thickness of HPTFs, a prompt mechanical control is designed based on eq. 2 for automatically adjusting r_r to counteract the fluctuation of r_d . The pitch number n is equal to how many turns substrate rotates in. GLAD is generally employed to create circular HPTFs (i.e. CHPTFs) and square HPTFs (i.e. SHPTFs), which are mainly reviewed in this work.

2.2 Growth mechanism²⁹

Initially, evaporated atoms undergo the vapor-to-solid phase transition and condense on a planar substrate. When the interaction among adatoms is larger than that between adatoms and the substrate, the condensation creates 3D nuclei in the

Volmer-Weber growth mode.³⁵ The nuclei randomly form on a planar substrate and have a wide distribution in sizes, because of the stochastic vapor condensation and random adatom diffusion on local topographies.³⁶ The glancing deposition imposes ballistic shadowing onto the nuclei, resulting in a larger amount of deposition on the nuclei than in shadowed regions (Scheme 1b). When $T_s < 0.3T_m$ (T_s : substrate temperature, T_m : melting point of deposited materials, in unit of Kelvin), it will be highly reduced the chance of adatom diffusion after the condensation on the tops of nuclei.³⁷ The shadowed regions will not be deposited with vaped atoms, and columnar structures will be formed out of nuclei. The shadowing effect basically relies on vapor collimation in linear trajectories, so as to require two counteracting factors: long throw distance from the vapor source (30-50 cm) to the substrate and no scattering of vaped atoms before condensation. Therefore, GLAD is generally carried out under high vacuum (10^{-7} - 10^{-5} Torr) to make the mean free path of vaped atoms longer than the long throw distance. The growth of spirals isn't homogenous but competitive. Within the growth, slow-evolving spirals will eventually fall into the shadowing regions of neighboring fast-growing springs, and extinct since they will no longer receive any vapor flux. To maintain constant planar density of deposited materials, the extinction of smaller spirals is accompanied by the broadening of fast-growing helices, as shown in Fig. 2b.

The prohibition of adatom diffusion into the shadowing regions is essential to create thin films with porous architectures and sculpture columnar shapes by controlling substrate movement, that is, $T_s < 0.3T_m$ should be satisfied. Without control over T_s in a typical GLAD setup, the high vacuum deposition system with poor heat dissipation causes T_s gradually increase to probably 200-300 °C, so that HPTFs are usually composed of high- T_m semiconductors, oxides and transition metals.^{32, 38-41}

Sculpturing low- T_m materials, e.g. noble metals, requires low-temperature deposition. Recently, the authors controll T_s as ~ 0 °C to generate Ag CHPTFs with P in the range of 100-350 nm (Fig. 2c), and Fischer *et al.* produced CHPTFs made of Au, Cu and Ag:Cu (65:35) with $P < 40$ nm at T_s of (-100) °C.³

An as-deposited random array of helices with a wide distribution in sizes results from the stochastic nucleation on planar surfaces (Fig. 1a-b). In order to improve the uniformity, a periodic array of uniform seeds is deposited before GLAD to function as initial nuclei for column growth.⁴² Careful control over the shape, size and spacing of the seeds leads to the growth of one column at each lattice point (Fig. 1c-d).^{24, 43} As a result, HPTFs duplicate the lattice patterns of the seeds. The pre-seeding process includes optical lithography,^{21, 44} electron-beam lithography,⁴⁵ laser-direct write lithography,⁴⁶ nanoimprint lithography,⁴⁷ micellar nanolithography,⁴⁸ nanosphere lithography,¹⁰ and self-assembly of nanospheres.⁴⁹

2.3 PhiSweep GLAD of SHPTFs

The random nucleation on a planar surface causes the competition among nuclei, extinction of small columns and broadening of growing columns, resulting in non-uniform columnar features along the substrate normal (Fig. 1b). The inhomogeneousness can be eliminated using PhiSweep GLAD.⁵⁰ Within the growth period of each arm of square helices, the substrate is swept from side to side about a central axis defining the direction of the straight arm, and one half of the angle covered by each sweep is called as the sweep angle. The substrate is paused for a period of time in the interval of Phi-sweeping, within which a certain, constant thickness of columns is evolved called as the sweep pitch. The PhiSweep decouples the directions of incident flux and column growth in GLAD, and effectively eliminates the arm broadening in SHPTFs (Fig. 1c-d).⁵¹

2.4 GLAD-templated fabrication

GLAD-generated HPTFs can function as a template to generate two kinds of PTFs. One is the helically perforated thin films that have helical pore architectures.⁵² The voids in oxide CHPTFs are filled with metals (e.g. Ni and Au) by electroplating or with polymers (e.g. polystyrene) via thermal melting and diffusion. The filled materials are partially etched to expose the top portions of template CHPTFs, followed by the selective removal of the template to generate a perforated thin film composed of the filled materials. The perforated thin films consist of a solid network with helical pores, rather than individual helical columns; and thus they are generally more robust than the template CHPTFs. Another is the tubular HPTFs, as shown in Fig. 3.⁵³ The template SiO_x CHPTFs (Fig. 3a) are conformally coated with amorphous Si by low-pressure chemical vapor deposition to create the core-shell structures (Fig. 3b). Ion-milling is operated to open a hole on the top of individual core-shell helices, followed by the removal of the core SiO_x using BOE (buffered oxide etch). The residue turns to be Si tubular CHPTFs (Fig. 3c).

3. Physical Properties

3.1 Surface areas

Krause *et al.* reported that mass density of TiO_2 CHPTFs has a slight decrease with α in the range of $50-65^\circ$, followed by an abrupt drop in the range of $65-85^\circ$.⁵⁴ The oblique deposition at $\alpha > 65^\circ$ effectively porosifies TiO_2 CHPTFs. Surface area was measured by the high-sensitivity Krypton gas adsorption at 77 K via the BET (Brunauer-Emmett-Teller) analysis. Surface area enhancement (SAE), calculated by normalizing surface area to the footprint area and thickness of TiO_2 CHPTFs, has a maximum of $\sim 900 \text{ m}^2/(\text{m}^2 \cdot \mu\text{m})$ at α of 65° . The slight increase of porosity with α in

the range of $50-65^\circ$ magnifies surface area, but the further porosification at $\alpha > 65^\circ$ reduce surface density of circular helices (i.e. the number of helices per unit area), accounting for the diminishing of surface area. Compared to TiO_2 vertical post PTFs, TiO_2 CHPTFs have smaller SAE when $\alpha < 65^\circ$ and $> 78^\circ$, but larger SAE at α in the range of $65-78^\circ$.

3.2 Mechanical properties

One of important mechanical properties of helices is the stiffness of CHPTFs or spring constant of individual spirals, which can be calculated from the slope of the plot of loading force versus displacement or deformation. Five-arm Si CHPTFs were deposited onto a bare Si(100), leading to the broadening of coils with the film growth. The stiffness was measured by atomic force microscope (AFM) as 407 N/m, which is enhanced to 510 N/m after heavy ion bombardment of 100 MeV Au^{8+} ion beam with an ion density of 10^{14} ions/cm².⁵⁵ To eliminate the broadening-induced non-uniformity, Si CHPTFs were deposited onto a Si(111) pre-patterned with silica spheres having diameter of 370 nm, resulting in a slight increase of stiffness to 439 N/m. The low-energy ion irradiation of 1.2 MeV Ar^{8+} can significantly magnify the stiffness to 1073 N/m. The two kinds of Si CHPTFs both exhibit a logarithmical increase of the stiffness with ionic energy density in the range of 10^2-10^4 eV/nm³. The stiffness has an increase of 32% at 10^4 eV/nm³ without any visible deformation, due to the ion bombardment-induced densification. The stiffness increases much faster beyond 10^4 eV/nm³ and has an enhancement of $\sim 250\%$ at 10^6 eV/nm³, ascribed to the anisotropic deformation initiated by nuclear energy losses.

Nanoindentation was applied to amorphous Si tubular CHPTFs, and spring constant of individual amorphous Si nanotubes was measured as 95 ± 32 N/m from the high-load portion of the unloading curves (Fig. 3d).⁵³ To avoid the deformation of the

underlying Si substrate, an indentation depth was chosen as one tenth of P . A coaxial spring model with broadening features was set up to simulate the spring constant as 79 N/m, in good agreement with the experimental measurement. The small hysteresis in Fig. 3d illustrates a minor plastic deformation. Multiple indentations performed at the same point show a series of nearly overlapping curves, indicating that the helical Si nanotubes may be reliably and repeatably deformed without structural damaging. A finite element analysis was carried out to simulate the elastic modulus of helically perforated thin films, finding out that the elastic modulus increases with the pitch angle ϑ (Fig. 2a), decreases with D and has a slight increase with coil spacing.⁵⁶ The elastic modulus of helically perforated thin films made of Ni was simulated as 162 GPa, in well agreement with the nanoindentation measurement of 154 GPa.

On a pre-patterned substrate Singh *et al.* deposited 4-turn Si SHPTFs that were then conformally coated with 10 nm Co, as a prototype of nanoelectromechanical actuators.⁵⁷ An actuator works in the principle that the current generates a magnetic field to produce magnetic forces between the coils and compress the spring. The coating of Co renders Si SHPTFs conductive, and a dc current was applied through individual Co-Si spirals by precisely loading a conducting AFM (CAFM) tip to contact individual spirals, and the current-induced compression displacement was monitored by CAFM. The compression displacement increases with current, reaching ~6 nm at 20 mA. The curve fitting evaluated the spring constant as 12 N/m, in good agreement with 8.75 ± 0.04 N/m directly measured by loading and unloading an AFM tip onto individual square spirals. Furthermore, the electric-mechanic-optic coupling imposes the function of interferometer onto CHPTFs ($n=2$, $P=300$ nm, $d \sim 70$ nm) made of tris(8-hydroxyquinoline) aluminum (Alq_3).⁷ The applied voltage compresses the Alq_3 helices, resulting in a blueshift of the optical transmission peak as 1.6 nm

(from 582.4 nm at 0 V to 580.8 nm at 10 V). Young's modulus was measured as 0.93 GPa, based on which the blueshift was simulated as 3.06 nm. The mismatch may be attributed to additional losses arising from electrical current between the contact electrodes.

3.3 Optical properties

GLAD creates chiral CHPTFs that have special optical response to the polarized light. Zhao *et al.* developed the technique of glancing angle co-deposition to generate composite PTFs in a shape of tilted rods, zigzag, vertical posts and circular spirals.⁵⁸ The host PTFs are made of polycrystalline MgF₂, and are embedded with face-centered cubic Ag nanoparticles with diameters of 10-20 nm. The volume ratio of Ag to MgF₂ is 1:10 in the composite PTFs. The absorption of s/p-polarized light was monitored in the wavelength (λ) range of 300-800 nm. Ag-plasmonic absorption at ~400 nm turns to be anisotropic when the hosts are the tilted and zigzag columns, but becomes isotropic when the hosts are the vertical posts and circular spirals. The discrete dipole approximation illuminates that the s/p-polarized differentiation originate from not only the size of Ag nanoparticles, but the alignment and interaction among Ag nanoparticles. Ag nanoparticles align along the longitudinal axis of the hosts, so their alignment duplicates the shape of MgF₂ hosts. The assembly of Ag nanoparticles on the tilted and zigzag columns is longer along the p-polarization direction than s-polarization, accounting for the redshift of the Ag plasmon peak from s- to p-polarization. The shape in vertical posts and circular spirals geometrically eliminate the differentiation of linear polarizations in the assembly direction, accounting for the isotropic plasmon absorption. When linearly polarized light is incident on CHPTFs along the helical axis, the transmitted light exhibits a rotation of the polarization plane, i.e. optical rotatory dispersion. Brett *et al.* deposited MgF₂

CHPTFs at α of 85° , and the optical rotation was measured to be anticlockwise for the right-handed CHPTFs and clockwise for the left-handed.⁵⁹ The optical rotation has a decay roughly with λ^{-4} when λ is longer than 550 nm.

It is of particular interest in studying the optical interaction of HPTFs to circular polarized light, i.e. left and right circular polarization (LCP and RCP). While composed of dielectrics, CHPTFs function as a circular Bragg filter that preferentially reflects circularly polarized light of the same handedness and transmits the opposite handedness.⁶⁰ The Bragg peak wavelength (λ_n^{Br}) is given by¹¹

$$\lambda_n^{Br} = P n_{avg} \quad (3)$$

in which n_{avg} is the average refractive index of CHPTFs, and P is the pitch. MgF₂ CHPTFs have P of ~ 350 nm, and the peak wavelength of differential transmission of LCP and RCP was calculated as 430.5 nm, matching well with the measured value of ~ 480 nm.⁶¹ The slight mismatch could be ascribed to some water absorption within the voids, leading to an increase of n_{avg} and the peak redshift. When the MgF₂ CHPTFs were impregnated with optical isotropic materials (e.g. water with n_{H_2O} of 1.33, chosen to closely match n_{MgF_2} of 1.38; and ethoxylated bisphenol diacrylate-SR349 with n_{SR349} of 1.56), all transmission difference was lost. It was concluded that chiral optical response arises from the scattering at the spiral/air interfaces. When the voids are filled with optically isotropic index-matching materials, the differential effect disappears. On the contrary, the optical circular differentiation retains while the voids are filled with optical anisotropic materials. It is interesting to find out that the combination of the two chirality in the bilayer TiO₂ CHPTFs effectively eliminates the circular selectivity due to the coupling of left and right handedness.⁶²

Simple employment of a shadow block enables one to deposit a spatially graded circular polarizer, composed of TiO₂ CHPTFs with an increasingly graded thickness

(or pitch) profile along the radial distance from the shadow block (Fig. 4a-c).⁶³ The right-handed CHPTFs preferentially transmit LCP and reflect RCP, leading to circular birefringence that generates a chiral polarization selective transmission peak (Fig. 4d). The transmission peak tends to redshift with an increase of the pitch along the radial distance from the shadow block (Fig. 4d), as predicted by eq. 3. The peak redshift becomes less with an increase of α , likely because the shadow cast by the shadow block is not as long as in the case of the more obliquely angled depositions. The circular polarization selectivity, i.e. the transmission peak intensity, reaches the maximum of $\sim 25\%$ at α of 70° (Fig. 4e). As evaluated by eq. 3, n_{avg} reduces with α from ~ 2 at α of 60° to ~ 1.55 at α of 80° , and is fairly constant in the graded TiO₂ CHPTFs. When CHPTFs are composed of plasmonic metals that are deposited at T_s far below $0.3T_m$, circular polarization significantly deviates from the Bragg theory. For example, when Au nanospirals deposited at $\sim (-100)^\circ\text{C}$ are dispersed in a solvent, they exhibit bisignate Cotton effect in circular dichroism (CD), and the change of spiral handedness alters the CD sign but barely shifts the peak position (Fig. 5a).³ The engineering of metallic materials can substantially tune the plasmonic resonance in the visible-near IR region (Fig. 5b). The study in chiral nanoplasmonics is still in its infant stage, and great effort should be input to clarify the mechanism.

SHPTFs are developed as 3D photonic crystals with adjustable band gap. In order to achieve the wafer-scale uniformity, SHPTFs were grown from pre-patterned periodic seeding arrays, and the PhiSweep technique was employed to eliminate the arm broadening.⁴⁵ At α of 86° , TiO₂ anatase SHPTFs were deposited onto a seeding array with a lattice space of 320 nm.⁴⁷ There are 8 sweeps per square spiral arm, and the ratio of lattice spacing, vertical pitch and spiral arm swing is $a:P:A=1:1.35:0.7$. The reflectivity measurement showed that the anatase SHPTFs have a pseudo-

bandgap centered at λ of ~ 600 nm, in good agreement with the finite difference electromagnetic simulation. The absence of a full 3D bandgap was attributed to the deviation of GLAD columns' cross-section from the optimal one, which has to be highly elongated in the deposition plane. A full 3D bandgap at λ of ~ 2 μm was achieved in Si SHPTFs with a [001]-diamond symmetry, P of 1330 ± 23 nm and D of 780 ± 36 nm.⁶⁴ The plane-wave-expansion simulation agreed well with the experimental result.

It is illuminated that helical dimensions (including P , D , d , n , ϑ , and lattice spacing) play a determining role on mechanical and optical properties of HPTFs, and on the functions of electric-mechanic-optic transformation, optical rotation and circular polarization. GLAD exhibits high degree of freedom in engineering the materials and dimensions of HPTFs, and thus provides a powerful fabrication platform to investigate helical properties and develop related applications.

4. Applications in green energy

Light-emitting diode (LED) is one important kind of energy-saving lighting. In the GaN-based LED, AlN CHPTFs act as a buffer layer and enhance the light output power with the injection current in the range of 5-100 mA, owing to the light scattering in CHPTFs and an increase in thermal conductivity of AlN (3.2 W/cm-K) superior to that of GaN (1.3 W/cm-K).⁶⁵ Solar cells convert solar energy to electricity, and need an antireflection coating (ARC) to reduce optical reflection loss and enhance irradiation absorption. In principle, ARC locates at the air/substrate interface and has refractive index (n_r) between that of air and the substrate.⁶⁶ For example, on a glass SiO₂ CHPTFs were deposited at r_r of 0.07 rpm, as function of α in the range of 0-85°.⁶⁷ n_r of SiO₂ CHPTFs decreases with α , owing to the α -induced porosification in

the CHPTFs. At α of 85° , the SiO_2 CHPTFs have porosity of 52% and n_r of 1.32 at λ of 550 nm. The tuning of n_r in-between 1 (n_r of the air) and ~ 1.5 (n_r of glasses) effectively reduces the average reflectance to 1.24% in λ of 400-800 nm. The mean transmittance of a slide glass coated with SiO_2 CHPTFs on both sides is approximately 97.5%.

Wong *et al.* employed TiO_2 anatase CHPTFs as a photoanode in dye-sensitized solar cells, since the porous structures have synergistic contribution in increasing surface areas for dye adsorption, enhancing charge transport in the photoanode, trapping solar irradiation and providing tight photoanode/dye interfaces to enhance the fill factor. Surface areas of 4 μm -thick anatase CHPTFs were maximized at α of 73° , resulting in the largest optical absorption of the adsorbed dyes (Fig. 6a).⁶⁸ As a result, J_{SC} was optimized as $6.0 \pm 0.1 \text{ mA/cm}^2$ and η as $2.78 \pm 0.08\%$ (Fig. 6b). When the length increases to 6 μm , the maximization is achieved in J_{SC} of 14.0 mA/cm^2 and η of 6.1%.⁶⁹ Compared to the regular DSSCs, CHPTFs don't improve photovoltaic performance, mainly ascribed to three issues. First, CHPTFs have close-packed structures to keep dyes from sufficiently diffusing in and making full use of the porous surface area. Second, there are large amount of surface defects on the helical surfaces, resulting in the trapping of photovoltaic charges. Surface modification with appropriate monolayers can effectively adjust the hydrophobicity/hydrophilicity to facilitate the conformal coating of CHPTFs with dyes, and to passivate surface defects. Third, charge mobility of the spiral columns should be optimized, e.g. by the during-GLAD doping with O_2 and post-GLAD annealing.

5. Prospects

Enantiomers are a pair of two stereoisomers with chiral configurations, and optically interact with LCP and RCP in a different way. The differential detection is monitored at two levels, including electronic transitions in the UV-visible region and molecular vibrations in the IR region. The chiral differentiation tends to be weak, mainly ascribed to the mismatch between the size of enantiomers and the electromagnetic wavelength. The mismatch becomes significantly severe in the long- λ IR region, so that the chiral differentiation intensity of molecular vibrations has roughly three orders of magnitude lower than that of electronic transitions. Plasmonic CHPTFs can locally enhance electromagnetic fields of LCP or RCP due to the chirality matching; hence it is promising to magnify the optically chiral differentiation. There are two stages to develop the emerging plasmonic CHPTFs for enantioselection. The first stage is to fundamentally study chiral plasmonics in the UV-visible-IR region, as function of spiral dimensions and materials. The second is to explore the mechanism of chiral coupling between enantiomers and local surface plasmon of CHPTFs for enhancing the enantioseparation selectivity and sensitivity.⁷⁰ The current research is just in the first stage and mainly focuses on the UV-visible-Near IR region in which molecular vibrations can barely be excited effectively. Therefore, a great effort should be made to develop this new technique, owing to optimal confidence in this technique with respect to three concerns. First, bioenantiomers generally have functional groups of -COOH, SH and NH, through which bioenantiomers can spontaneously adsorb to CHPTFs composed of noble metals via self-assembly. The spontaneous covalent adsorption could significantly reduce the detection duration. Second, the flexible engineering of spiral dimensions and materials in GLAD can adjust local surface plasmon and tune the chiral coupling, leading to the enhancement of enantioselection for a wide variety of bioenantiomers.

Third, the improvement of enantioseparation sensitivity makes it possible to carry out dynamic analyses in biological cultures.

It can be further devoted to exploring the mechanic-derived applications. For instance, electrostatic compression of soft CHPTFs results in a precise control over the transmission peak wavelength, based on which a movable mirror element for microelectrochemical devices or a pressure sensitive optical transducer can be generated. Another example is to direct the movement of magnetic spirals via wireless control. Fischer *et al.* created silica helices that were thermally evaporated with ~ 30 nm Co to cover one-half of helices.⁷¹ The magnetic spirals can be propelled wirelessly in water with micrometer-scale precision using homogeneous magnetic fields, and the rotation about the longitudinal axis is favored. The propulsion speed is $14 \mu\text{m/s}$ under 60 G magnetic field rotating at 66 Hz in the plane orthogonal to its direction of translation, and increases to $\sim 40 \mu\text{m/s}$ at ~ 150 Hz. A wide range of applications could be derived from the magnetic propellers, such as carrying chemicals, delivering drugs, pushing loads, and acting as local probes in rheological measurements.

At the end, it is of practical interest to discuss how to realize mass production of GLAD. Up to date, it is still in the laboratory's scale to study and develop the GLAD technique. It usually takes a few hours to deposit a wafer per time. Owing to the long deposition distance and large- α -induced small projection area of a wafer towards the evaporated flux, only a small portion of evaporated materials condense on the wafer. Mass production could be realized by two steps. The first is to increase the number of wafers in a deposition batch. With a center at the evaporating source, a conical geometry provides identical deposition distance and α along the circumference of its cross-section. Multiple substrates can be installed along the cone's cross-section for GLAD. The longer the deposition distance, the more substrates can be installed.

Multiple reflection of condensed vapors among substrates should be eliminated by installing shutters at appropriate positions. The second step is the roll-to-roll GLAD, which was currently proposed by Brett *et al.* They came up with a prototype of three-gear/roller system that could be mated to the existing substrate rotation motor with minimal cost, and demonstrated the deposition of several core GLAD structures.⁷² There are several areas of future studies required for the roll-to-roll GLAD, including the determining the relationship between as-deposited and target α , redesigning the deposition chamber to remove geometrical limitations in the roller space, optimizing the structure uniformity and reproducibility, and using substrate cooling systems to adopt flexible polymer substrates in the roll-to-roll GLAD.

Acknowledgement:

We acknowledge financial support by HKBU8/CRF/11E (F Bai) and Faculty of Science at HKBU.

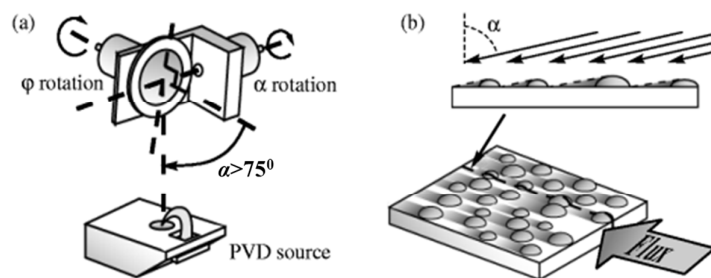
References:

1. M. Yang and N. A. Kotov, *J. Mater. Chem.*, 2011, **21**, 6775-6792.
2. Q. Zhou, Y. P. He, J. Abell, Z. J. Zhang and Y. P. Zhao, *J. Phys. Chem. C*, 2011, **115**, 14131-14140.
3. A. G. Mark, J. G. Gibbs, T. C. Lee and P. Fischer, *Nat. Mater.*, 2013, **12**, 802-807.
4. K. Robbie, G. Beydaghyan, T. Brown, C. Dean, J. Adams and C. Buzea, *Rev. Sci. Instrum.*, 2004, **75**, 1089-1097.
5. G. K. Kannarpady, K. R. Khedir, H. Ishihara, J. Woo, O. D. Shin, S. Trigwell, C. Ryerson and A. S. Biris, *ACS Appl. Mater. Interfaces*, 2011, **3**, 2332-2340.
6. C. Khare, J. W. Gerlach, M. Weise, J. Bauer, T. Hoche and B. Rauschenbach, *Phys. Status Solidi A-Appl. Mat.*, 2011, **208**, 851-856.
7. G. D. Dice, M. J. Brett, D. Wang and J. M. Buriak, *Appl. Phys. Lett.*, 2007, **90**, 253101.
8. M. Thomas, B. J. Worfolk, D. A. Rider, M. T. Taschuk, J. M. Buriak and M. J. Brett, *ACS Appl. Mater. Interfaces*, 2011, **3**, 1887-1894.
9. J. G. Van Dijken, M. D. Fleischauer and M. J. Brett, *Org. Electron.*, 2011, **12**, 2111-2119.
10. C. Patzig, T. Karabacak, B. Fuhrmann and B. Rauschenbach, *J. Appl. Phys.*, 2008, **104**, 094318.
11. L. X. Hu, P. Wang, X. Y. Wan and S. J. Jiang, *J. Mater. Sci. Technol.*, 2012, **28**, 97-102.
12. R. Alvarez, L. Gonzalez-Garcia, P. Romero-Gomez, V. Rico, J. Cotrino, A. R. Gonzalez-Elipe and A. Palmero, *J. Phys. D-Appl. Phys.*, 2011, **44**, 385302.
13. S. R. Kennedy, J. C. Sit, D. J. Broer and M. J. Brett, *Liq. Cryst.*, 2001, **28**, 1799-1803.
14. J. Wannemacher, S. R. Jim, M. T. Taschuk, M. J. Brett and G. E. Morlock, *J. Chromatogr. A*, 2013, **1318**, 234-243.
15. J. Ni, Y. Zhu, S. H. Wang, Z. C. Li, Z. J. Zhang and B. Q. Wei, *J. Am. Ceram. Soc.*, 2009, **92**, 3077-3080.
16. C. C. Jaing, *Appl. Optics*, 2011, **50**, C159-C163.
17. J. M. La Forge, T. L. Cocker, A. L. Beaudry, K. Cui, R. T. Tucker, M. T. Taschuk, F. A. Hegmann and M. J. Brett, *Nanotechnology*, 2014, **25**.
18. N. J. Ku, J. H. Huang, C. H. Wang, H. C. Fang and C. P. Liu, *Nano Lett.*, 2012, **12**, 562-568.
19. W. Smith, A. Wolcott, R. C. Fitzmorris, J. Z. Zhang and Y. P. Zhao, *J. Mater. Chem.*, 2011, **21**, 10792-10800.
20. S. V. Kesapragada, P. R. Sotherland and D. Gall, *J. Vac. Sci. Technol. B*, 2008, **26**, 678-681.
21. D. X. Ye, T. Karabacak, B. K. Lim, G. C. Wang and T. M. Lu, *Nanotechnology*, 2004, **15**, 817-821.
22. Y. Hu, Z. J. Zhang, Q. Zhou, W. Liu, Z. C. Li and D. Q. Meng, *Nano Res.*, 2010, **3**, 438-443.
23. D. H. Choi, Y. D. Han, B. K. Lee, S. J. Choi, H. C. Yoon, D. S. Lee and J. B. Yoon, *Adv. Mater.*, 2012, **24**, 4408-4413.
24. D. X. Ye, C. L. Ellison, B. K. Lim and T. M. Lu, *J. Appl. Phys.*, 2008, **103**, 103531.
25. R. B. Patel, M. C. Gopani and M. R. Patel, *Chromatogr.*, 2013, **76**, 1225-1231.

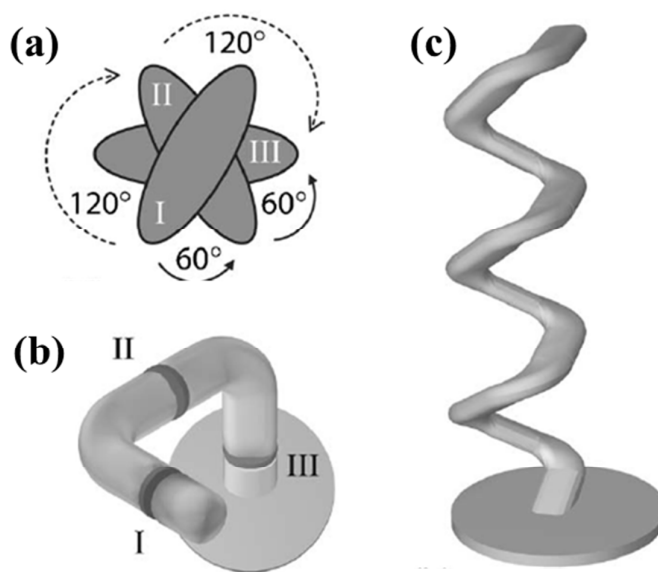
26. M. Mitov, *Adv. Mater.*, 2012, **24**, 6260-6276.
27. Y. P. He and Y. P. Zhao, *Nanoscale*, 2011, **3**, 2361-2375.
28. X. D. Xiao, G. P. Dong, H. Yu, Z. X. Fan, H. B. He and J. D. Shao, *Rare Metal Mater. Eng.*, 2008, **37**, 1317-1322.
29. M. M. Hawkeye and M. J. Brett, *J. Vac. Sci. Technol. A-Vac. Surf. Films*, 2007, **25**, 1317-1335.
30. J. J. Steele and M. J. Brett, *J. Mater. Sci.-Mater. Electron.*, 2007, **18**, 367-379.
31. M. J. Brett and M. M. Hawkeye, *Science*, 2008, **319**, 1192-1193.
32. K. Robbie and M. J. Brett, *J. Vac. Sci. Technol. A-Vac. Surf. Films*, 1997, **15**, 1460-1465.
33. A. C. van Popta, M. J. Brett and J. C. Sit, *J. Appl. Phys.*, 2005, **98**, 083517.
34. C. Patzig, A. Miessler, T. Karabacak and B. Rauschenbach, *Phys. Sta. Solidi B-Basic Solid State Phys.*, 2010, **247**, 1310-1321.
35. K. Reichelt, *Vacuum*, 1988, **38**, 1083-1099.
36. C. Ratsch and J. A. Venables, *J. Vac. Sci. Technol. A*, 2003, **21**, S96-S109.
37. W. F. Lau, F. Bai and Z. F. Huang, *Nanotechnology*, 2013, **24**, 465707.
38. C. Patzig and B. Rauschenbach, *J. Vac. Sci. Technol. A*, 2008, **26**, 881-886.
39. S. V. Kesapragada, P. Victor, O. Nalamasu and D. Gall, *Nano Lett.*, 2006, **6**, 854-857.
40. Q. Zhou, Z. C. Li, J. Ni and Z. J. Zhang, *Mater. Trans.*, 2011, **52**, 469-473.
41. J. B. Sorge, M. T. Taschuk, N. G. Wakefield, J. C. Sit and M. J. Brett, *J. Vac. Sci. Technol. A*, 2012, **30**, 021507.
42. M. Malac, R. F. Egerton, M. J. Brett and B. Dick, *J. Vac. Sci. Technol. B*, 1999, **17**, 2671-2674.
43. M. O. Jensen and M. J. Brett, *IEEE Trans. Nanotechnol.*, 2005, **4**, 269-277.
44. M. W. Horn, M. D. Pickett, R. Messier and A. Lakhtakia, *Nanotechnology*, 2004, **15**, 303-310.
45. M. A. Summers, K. Tabunshchyk, A. Kovalenko and M. J. Brett, *Phot. Nanostruct. Fund. Appl.*, 2009, **7**, 76-84.
46. M. O. Jensen and M. J. Brett, *J. Nanosci. Nanotechnol.*, 2005, **5**, 723-728.
47. J. D. Krabbe, V. Leontyev, M. T. Taschuk, A. Kovalenko and M. J. Brett, *J. Appl. Phys.*, 2012, **111**, 064314.
48. R. Glass, M. Moller and J. P. Spatz, *Nanotechnology*, 2003, **14**, 1153-1160.
49. C. M. Zhou and D. Gall, *Thin Solid Films*, 2006, **515**, 1223-1227.
50. M. O. Jensen and M. J. Brett, *Appl. Phys. A-Mater. Sci. Process.*, 2005, **80**, 763-768.
51. D. X. Ye, T. Karabacak, R. C. Picu, G. C. Wang and T. M. Lu, *Nanotechnology*, 2005, **16**, 1717-1723.
52. A. L. Elias, K. D. Harris and M. J. Brett, *J. Microelectromech. Syst.*, 2004, **13**, 808-813.
53. Z. F. Huang, K. D. Harris and M. J. Brett, *Adv. Mater.*, 2009, **21**, 2983-2987.
54. K. M. Krause, M. T. Taschuk, K. D. Harris, D. A. Rider, N. G. Wakefield, J. C. Sit, J. M. Buriak, M. Thommes and M. J. Brett, *Langmuir*, 2010, **26**, 4368-4376.
55. R. Nagar, B. R. Mehta, J. P. Singh, C. Patzig, B. Rauschenbach and D. Kanjilal, *J. Appl. Phys.*, 2010, **107**, 094315.
56. S. P. Fernando, A. L. Elias and M. J. Brett, *J. Mater. Res.*, 2006, **21**, 1101-1105.
57. J. P. Singh, D. L. Liu, D. X. Ye, R. C. Picu, T. M. Lu and G. C. Wang, *Appl. Phys. Lett.*, 2004, **84**, 3657-3659.

58. Y. P. He, Z. Y. Zhang, C. Hoffmann and Y. P. Zhao, *Adv. Funct. Mater.*, 2008, **18**, 1676-1684.
59. K. Robbie, M. J. Brett and A. Lakhtakia, *Nature*, 1996, **384**, 616.
60. A. Lakhtakia and M. W. McCall, *J. Mod. Opt.*, 2002, **49**, 1525-1535.
61. K. Robbie, D. J. Broer and M. J. Brett, *Nature*, 1999, **399**, 764-766.
62. Y. J. Park, K. M. A. Sobahan, J. J. Kim and C. K. Hwangbo, *J. Opt. Soc. Korea*, 2009, **13**, 218-222.
63. K. M. Krause and M. J. Brett, *Adv. Funct. Mater.*, 2008, **18**, 3111-3118.
64. D. X. Ye, Z. P. Yang, A. S. P. Chang, J. Bur, S. Y. Lin, T. M. Lu, R. Z. Wang and S. John, *J. Phys. D-Appl. Phys.*, 2007, **40**, 2624-2628.
65. L. C. Chen, C. H. Tien, X. G. Liu and B. S. Xu, *J. Nanomater.*, 2012, **2012**, 409123.
66. Z. F. Huang, M. M. Hawkeye and M. J. Brett, *Nanotechnology*, 2012, **23**, 275703.
67. Y. J. Park, K. M. A. Sobahan, J. J. Kim and C. K. Hwangbo, *J. Korean Phys. Soc.*, 2009, **55**, 2634-2637.
68. H. Y. Yang, M. F. Lee, C. H. Huang, Y. S. Lo, Y. J. Chen and M. S. Wong, *Thin Solid Films*, 2009, **518**, 1590-1594.
69. M. S. Wong, M. F. Lee, C. L. Chen and C. H. Huang, *Thin Solid Films*, 2010, **519**, 1717-1722.
70. E. Hendry, T. Carpy, J. Johnston, M. Popland, R. V. Mikhaylovskiy, A. J. Laphorn, S. M. Kelly, L. D. Barron, N. Gadegaard and M. Kadodwala, *Nat. Nanotechnol.*, 2010, **5**, 783-787.
71. A. Ghosh and P. Fischer, *Nano Lett.*, 2009, **9**, 2243-2245.
72. K. M. Krause, M. T. Taschuk and M. J. Brett, *J. Vac. Sci. Technol. A*, 2013, **31**, 031507.

Schemes and Figures:



Scheme 1. Schematic of (a) GLAD and (b) GLAD-induced ballistic shadowing of the random nuclei.



Scheme 2. (a) A triangle helix can be described as a stack of biaxial plates that rotate by $360^\circ/3=120^\circ$ increments. Schematic of (b) the top-view of a single-turn triangle helix and (c) individual triangle helix with multiple turns. (Adapted from Ref. 33. Copyright 2005 American Institute of Physics)

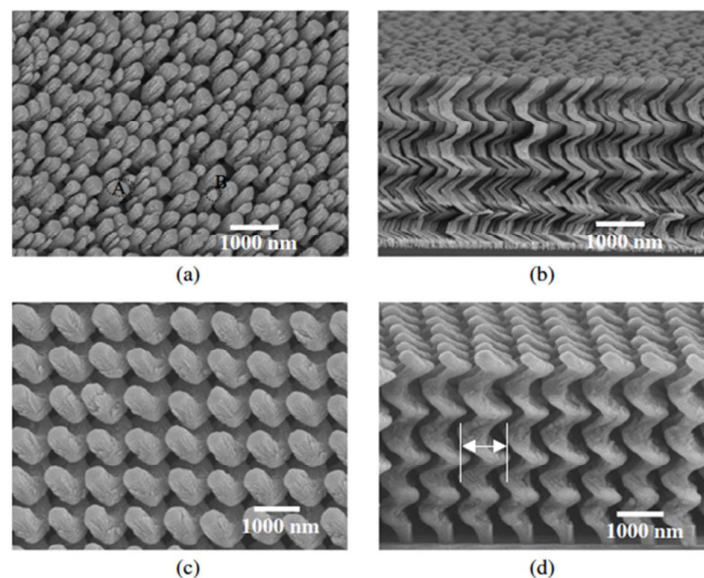


Figure 1. The PhiSweep GLAD (α of 85° , and the sweep angle of 30°) of Si SHPTFs on (a, b) a bare and (c, d) pre-patterned Si(100) wafer. (a, c) SEM top-view images, and (b, d) cross-sectional images. (Adapted from Ref. 51. Copyright 2005 Institute of Physics Science)

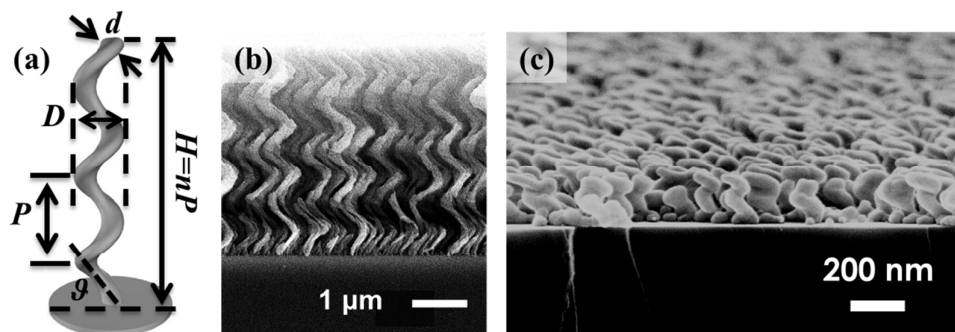


Figure 2. (a) Schematic of a circular helix, having a set of dimensional parameters including the height (H), pitch (P), the number of pitch (n), coil diameter (D), cross-section diameter (d) and pitch angle (ϑ). GLAD of CHPTFs operated in the authors' laboratory at HKBU: (b) a SEM cross-sectional image of SiO_x deposited at α of 87° , without control over T_s ; (c) a SEM oblique image of Ag CHPTFs deposited at α of 86° and T_s of $\sim 0^\circ\text{C}$. (a) Adapted from Ref. 33. Copyright 2005 American Institute of Physics.

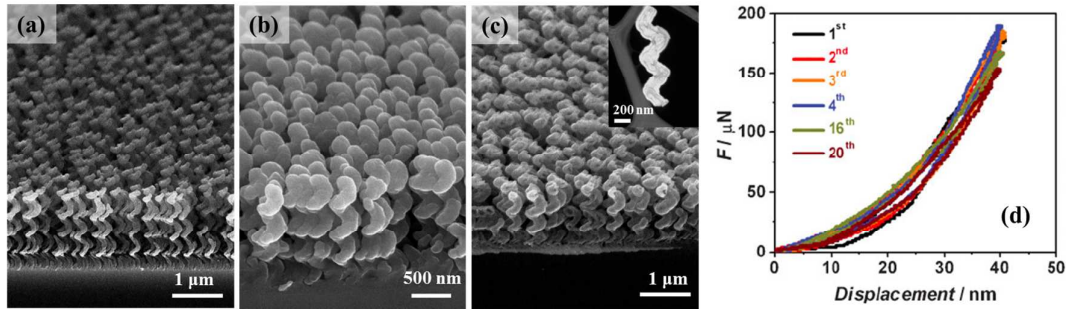


Figure 3. The GLAD-templated fabrication of Si tubular CHPTFs: (a) the template of SiO_x CHPTFs; (b) the core-shell Si-SiO_x CHPTFs; (c) the Si tubular CHPTFs after the removal of the core SiO_x. (a-c) SEM oblique-view images; the inset in (c) is a TEM image of a Si spiral tube. (d) The force-displacement curves monitored from repeated nanoindentation up to 20 times at one spot of the Si tubular CHPTFs. (Adapted from Ref. 53. Copyright 2009 Wiley-VCH)

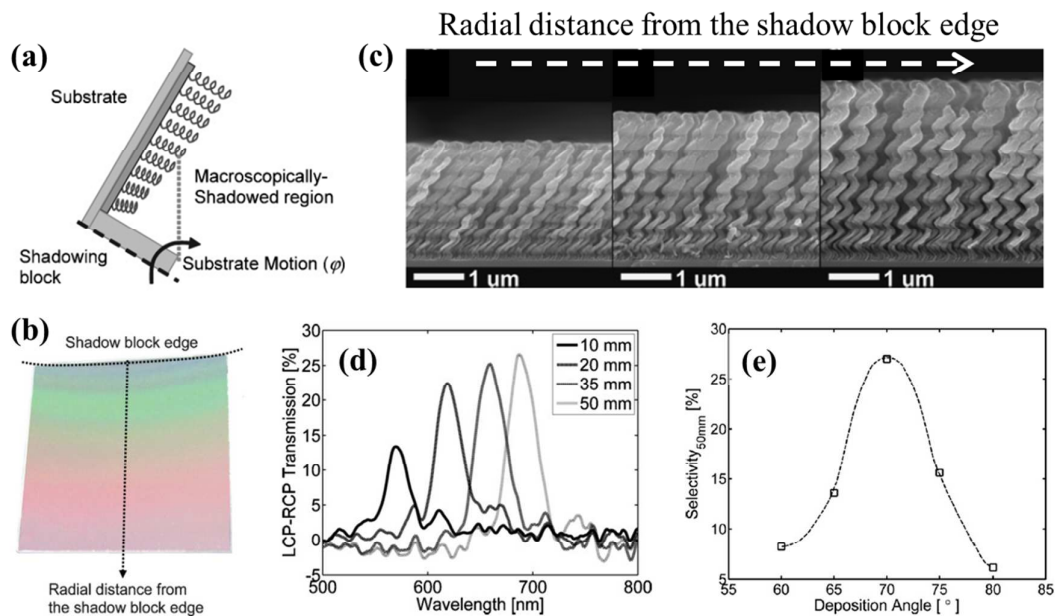


Figure 4. GLAD with a shadowing block to deposit a spatially graded circular polarizer. (a) Schematic of the deposition setup. (b) A photograph of a graded right-handed TiO₂ CHPTF. (c) SEM cross-sectional images of right-handed TiO₂ CHPTFs deposited at different positions along the radial distance from the shadow block edge (α of 85⁰). (d) The circular selective transmission spectra of the graded CHPTFs, deposited at α of 70⁰. (e) A plot of circular selectivity with α , at the radial distance of 50 mm from the shadow block edge. (Adapted from Ref. 63. Copyright 2008 Wiley-VCH)

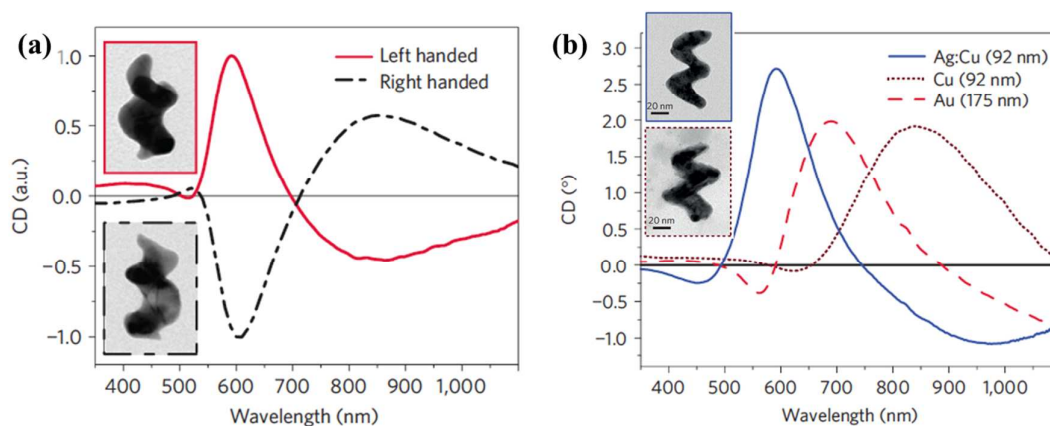


Figure 5. CD of plasmonic nanospirals deposited by GLAD at T_s of as low as (-170 °C). CD is defined as the optical absorption difference between LCP and RCP: (a) Au nanospirals with left and right handedness, P of 34 nm and n of 2 turns; (b) left-handed plasmonic nanospirals made of different metals. The number in unit of nm shown in the legend represents H of spirals. (Adapted from Ref. 3. Copyright 2013 Nature Publishing Group)

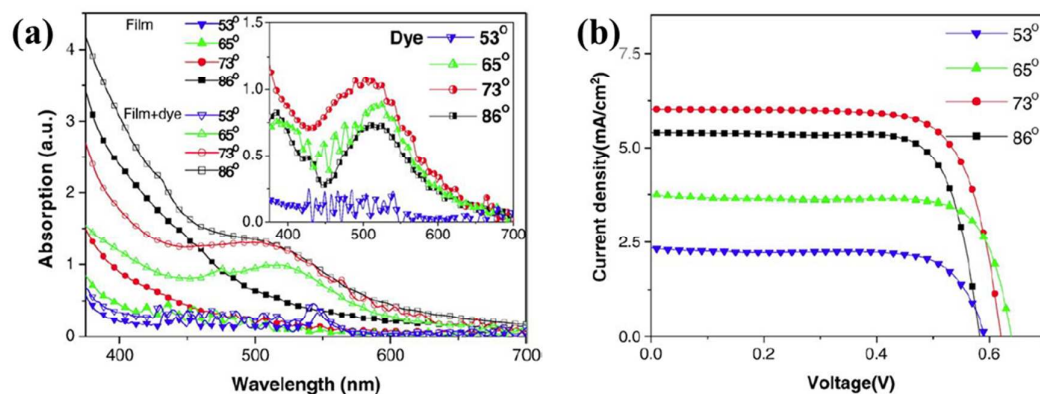


Figure 6. (a) UV-visible absorption spectra of TiO_2 anatase CHPTFs without (solid lines) and with dye absorption (dotted lines). (b) I-V photovoltaic measurements of the dye-sensitized solar cells having TiO_2 anatase CHPTFs as the photoanode, as function of α in the range of 53 - 86 °. (Adapted from Ref. 68. Copyright 2009 Elsevier)